Strong interlayer coupling in van der Waals heterostructures built from single-layer chalcogenides

Hui Fang[a,b], Corsin Battaglia[a,b], Carlo Carraro[c], Slavomir Nemsak[b,d], Burak Ozdol[e,f], Jeong Seuk Kang[a,b], Hans A. Bechtel[g], Sujay B. Desai[a,b], Florian Kronast[h], Ahmet A. Unal[h], Giuseppina Conti[b,d], Catherine Conlon[b,d], Gunnar K. Palsson[b,d], Michael C. Martin[g], Andrew M. Minor[e,f], Charles S. Fadley[b,d], Eli Yablonovitch[a,b,1], Roya Maboudian[c], and Ali Javey[a,b,1]

Departments of [a]Electrical Engineering and Computer Sciences, [c]Chemical and Biomolecular Engineering, and [e]Materials Science and Engineering, University of California, Berkeley, CA 94720; [b]Materials Sciences Division, [f]National Center for Electron Microscopy, and [g]Advanced Light Source, Lawrence Berkeley National Laboratory, Berkeley, CA 94720; [d]Department of Physics, University of California, Davis, CA 95616; and [h]Helmholtz-Zentrum Berlin für Materialien und Energie GmbH, D-12489 Berlin, Germany

Contributed by Eli Yablonovitch, March 24, 2014 (sent for review March 10, 2014)

Semiconductor heterostructures are the fundamental platform for many important device applications such as lasers, light-emitting diodes, solar cells, and high-electron-mobility transistors. Analogous to traditional heterostructures, layered transition metal dichalcogenide heterostructures can be designed and built by assembling individual single layers into functional multilayer structures, but in principle with atomically sharp interfaces, no interdiffusion of atoms, digitally controlled layered components, and no lattice parameter constraints. Nonetheless, the optoelectronic behavior of this new type of van der Waals (vdW) semiconductor heterostructure is unknown at the single-layer limit. Specifically, it is experimentally unknown whether the optical transitions will be spatially direct or indirect in such hetero-bilayers. Here, we investigate artificial semiconductor heterostructures built from single-layer WSe_2 and MoS_2. We observe a large Stokes-like shift of ∼100 meV between the photoluminescence peak and the lowest absorption peak that is consistent with a type II band alignment having spatially direct absorption but spatially indirect emission. Notably, the photoluminescence intensity of this spatially indirect transition is strong, suggesting strong interlayer coupling of charge carriers. This coupling at the hetero-interface can be readily tuned by inserting dielectric layers into the vdW gap, consisting of hexagonal BN. Consequently, the generic nature of this interlayer coupling provides a new degree of freedom in band engineering and is expected to yield a new family of semiconductor heterostructures having tunable optoelectronic properties with customized composite layers.

MoS_2-WSe_2 heterostructure | Moiré pattern | charge transfer | exciton relaxation | rectifying

Two-dimensional layered transition metal dichalcogenide (TMDC) semiconductors such as MoS_2 and WSe_2 have established themselves as strong contenders for next-generation electronics and optoelectronics (1–6) and are promising building blocks for novel semiconductor heterostructures (7–11). Conventional heterostructures are mainly based on group IV, III-V, or II-VI semiconductors with covalent bonding between atoms at the hetero-interface. Owing to atomic interdiffusion during growth, the resulting atomic-scale interface roughness and composition variation at the hetero-interface inevitably smear the density of states profile and consequently compromise the performance of these heterostructures, especially as the film thicknesses are reduced toward a single atomic layer. In addition, the choice of material components for conventional heterostructures is strongly dictated by lattice mismatch.

In TMDCs, however, individual layers are held together by van der Waals (vdW) forces, without surface dangling bonds (12). Semiconductor heterostructures built up from monolayer TMDCs would in principle offer atomically regulated interfaces and thereby sharp band edges. Theoretical studies have predicted different electronic structures and optical properties from TMDC hetero-bilayers (13–17); however, to date there have been no experimental results. Whereas previous experimental efforts have focused on graphene-based layered heterostructures (8–11, 18–26), we present an experimental study on the electronic interlayer interaction in a heterostructure built from two single-layer TMDC semiconductors, namely, MoS_2 and WSe_2. The hetero-bilayers are characterized by transmission electron microscopy, X-ray photoelectron microscopy, electron transport studies, and optical spectroscopy to elucidate the band alignments, optoelectronic properties, and the degree of the electronic layer coupling in this novel material system.

The fabrication of WSe_2/MoS_2 hetero-bilayers was realized by stacking individual monolayers on top of each other (see *SI Methods* for details). Fig. 1*A* shows an illustration of the hetero-bilayer, and Fig. 1*B* displays the corresponding optical microscope image of a WSe_2/MoS_2 hetero-bilayer on a Si substrate with 260-nm thermally grown SiO_2. Owing to the 3.8% lattice mismatch, estimated from the bulk lattice constants (12), as well as the unregulated, but in principle controllable, angular alignment (ϕ) between the constituent layers, the heterostructure lattice forms a moiré pattern, clearly visible in the high-resolution transmission electron microscopy (HRTEM) image in Fig. 1*C*. The HRTEM image displays the boundary region between

Significance

A new class of heterostructures consisting of layered transition metal dichalcogenide components can be designed and built by van der Waals (vdW) stacking of individual monolayers into functional multilayer structures. Nonetheless, the optoelectronic properties of this new type of vdW heterostructure are unknown. Here, we investigate artificial semiconductor heterostructures built from single-layer WSe_2 and MoS_2. We observe spatially direct absorption but spatially indirect emission in this heterostructure, with strong interlayer coupling of charge carriers. The coupling at the hetero-interface can be readily tuned by inserting hexagonal BN dielectric layers into the vdW gap. The generic nature of this interlayer coupling is expected to yield a new family of semiconductor heterostructures having tunable optoelectronic properties through customized composite layers.

Author contributions: H.F., C. Carraro, R.M., and A.J. designed research; H.F., C. Carraro, S.N., B.O., J.S.K., H.A.B., S.B.D., F.K., A.A.U., G.C., C. Conlon, G.K.P., and M.C.M. performed research; H.F., C.B., C. Carraro, S.N., B.O., G.C., A.M.M., C.S.F., E.Y., R.M., and A.J. analyzed data; and H.F., C.B., and A.J. wrote the paper.

The authors declare no conflict of interest.

Freely available online through the PNAS open access option.

[1]To whom correspondence may be addressed. E-mail: eliy@eecs.berkeley.edu or ajavey@eecs.berkeley.edu.

This article contains supporting information online at www.pnas.org/lookup/suppl/doi:10.1073/pnas.1405435111/-/DCSupplemental.

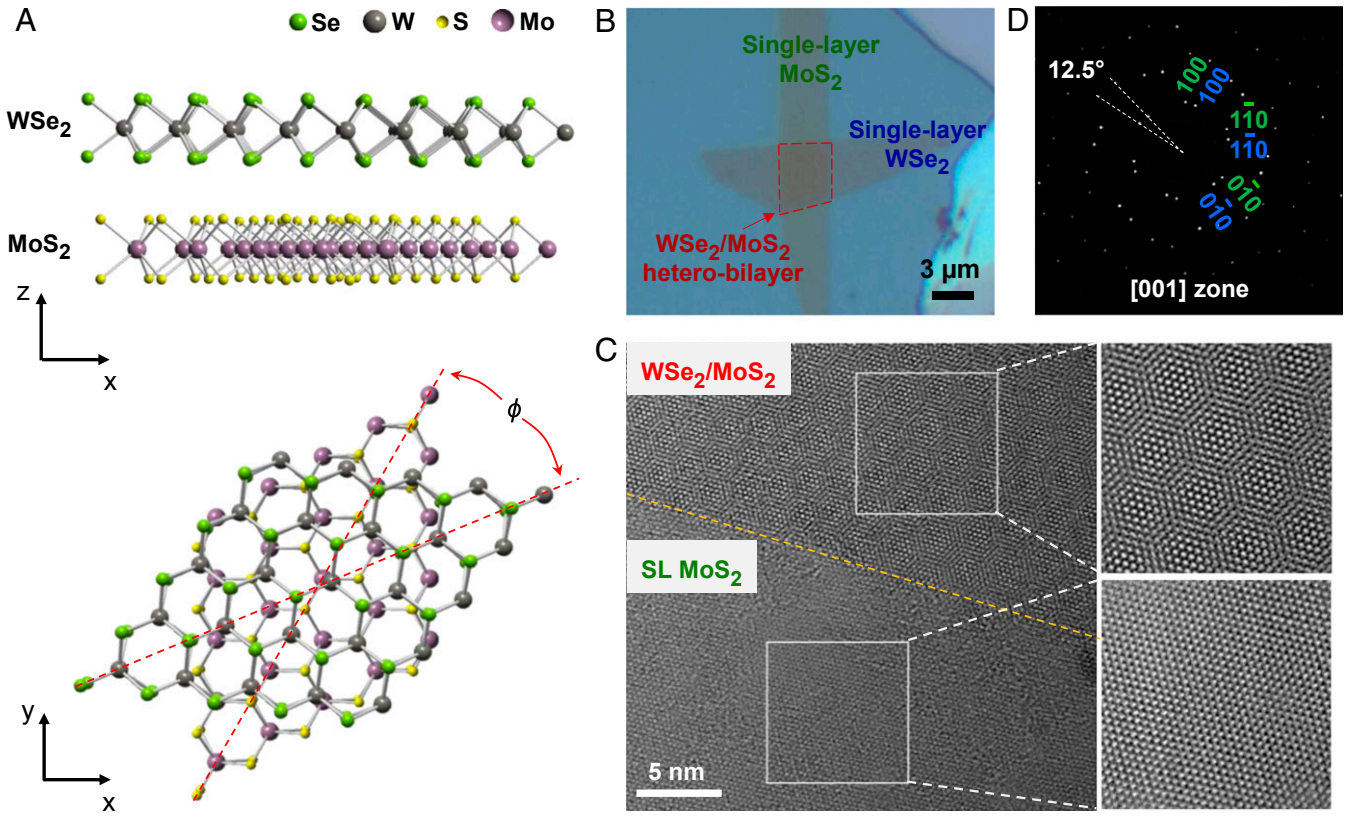

Fig. 1. WSe_2/MoS_2 hetero-bilayer illustration, optical image, and TEM images. (*A*) Atomistic illustrations of the heterostructure of single-layer (SL) WSe_2 on SL MoS_2 with their respective lattice constants and a misalignment angle ϕ. (*B*) Optical microscope image of a WSe_2/MoS_2 hetero-bilayer on a Si/SiO_2 substrate (260-nm SiO_2). (*C*) HRTEM images of a boundary region of SL MoS_2 and the hetero-bilayer, showing the resulting Moiré pattern. (*D*) The electron diffraction pattern of the hetero-bilayer shown in *B*, with the pattern of MoS_2 and WSe_2 indexed in green and blue colors, respectively.

single-layer MoS_2 and the WSe_2/MoS_2 hetero-bilayer. Whereas MoS_2 exhibits a simple hexagonal lattice, the heterostructure shows moiré fringes with a spatial envelope periodicity on the order of four to six times the lattice constants of WSe_2 (or MoS_2). Inspection of the diffraction pattern in Fig. 1*D* along the [001] zone axis reveals that in this particular sample the two hexagonal reciprocal lattices are rotated by ϕ=12.5° with respect to each other and there is negligible strain in the two constituent layers (*Supporting Information*). The alignment of the two lattices can also be examined with a fast Fourier transform of the two zoomed-in TEM images in Fig. 1*C* (Fig. S1). The absence of strain in the constituent layers of the WSe_2/MoS_2 hetero-bilayer is also confirmed by Raman spectroscopy (Fig. S2), which show that the in-plane vibration modes of both WSe_2 and MoS_2 maintain their corresponding positions before and after transfer.

To shed light on the electronic structure of the WSe_2/MoS_2 heterostack, we performed X-ray photoelectron spectroscopy (XPS). Specifically, we used a photoemission electron microscope (PEEM) with a high spatial resolution of 30 nm to discriminate between photoelectrons emitted from the WSe_2 single layer, MoS_2 single layer, and the WSe_2/MoS_2 hetero-bilayer, as illustrated in Fig. 2*A* (see Fig. S3 for details). In addition, by looking at the core-level photoelectrons, we achieved elemental and electronic selectivity that allows us to probe photoelectrons originating from the top layer of the hetero-bilayer and to directly quantify the potential difference between the WSe_2 layer in the hetero-stack with respect to the WSe_2 single-layer reference on the substrate. As shown in Fig. 2*B*, a peak shift of about −220 meV in binding energy (or +220 meV in kinetic energy) is evident in the W 4f core levels of the hetero-bilayer compared with the WSe_2 single layer. The direction of the peak shift is consistent with a negative net charge on the WSe_2 in the WSe_2/MoS_2 hetero-bilayer. However, a shift of +190 meV is observed in the Mo 3d core levels of the WSe_2/MoS_2 in Fig. 2*C*. Our PEEM results therefore indicate that the WSe_2 layer has a negative net charge, whereas the MoS_2 layer has a positive net charge as a result of contact potential. The hetero-bilayer can essentially be interpreted as being a 2D dipole, an atomically thin parallel plate capacitor with vdW gap with a built-in potential up to 400 meV, originating from the work function difference induced charge transfer between the two constituent single layers. The latter interpretation is also consistent with the p- and n-type character of WSe_2 and MoS_2, respectively (2, 3).

To investigate the optoelectronic properties of the WSe_2/MoS_2 hetero-bilayer, we used photoluminescence (PL) and absorption spectroscopy. It is known that both single-layer WSe_2 and MoS_2 exhibit direct band gaps, whereas their bulk and homo-bilayer counterparts are indirect (1, 27). In agreement with previous work we observe strong excitonic PL peaks at 1.64 eV and 1.87 eV for single-layer WSe_2 and MoS_2, respectively (Fig. 3*A*). Note that single-layer WSe_2 shows a 10–20 times higher PL intensity than single-layer MoS_2, a result consistent with ref. 28. For the WSe_2/MoS_2 hetero-bilayer, we observe a peak at 1.55 eV, lying interestingly at a lower energy than for the two constituent single layers, as shown in Fig. 3*A* (with intensity ∼1.5 times higher than for single-layer MoS_2). The appearance of a peak at such low energy was observed consistently for multiple (>10) samples, with peak energies ranging from 1.50 to 1.56 eV (Fig. S4). This distribution is attributed to sample-to-sample variations in interface quality and/or alignment angle ϕ. Of value in optoelectronics, an Urbach tail inverse slope, corresponding to the band edge sharpness of ∼30 meV/dec is extracted

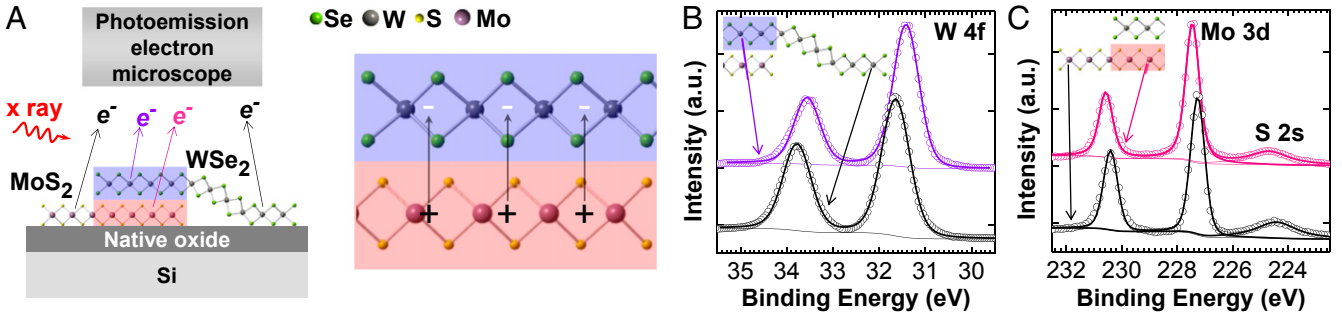

Fig. 2. XPS core level shift analyses of WSe_2/MoS_2 heterostructures. (*A*) Sketch of the spatially resolved PEEM experiment. (*B*) Comparison of W 4f core level doublet from WSe_2 and WSe_2/MoS_2 indicating a 220-meV shift to lower binding energy, corresponding to a negative net charge on the WSe_2 top layer. (*C*) Comparison of Mo 3d core level doublet and S 2s singlet from MoS_2 and WSe_2/MoS_2 indicating a shift of 190 meV to higher binding energy, corresponding to a positive net charge on MoS_2. The single peak at 224.4–224.6 eV is identified as S 2s, which shows the same shift as Mo 3d, as expected.

from the PL spectra (29, 30) (Fig. S5). The steep tail slopes of our hetero-bilayer prove that high-quality heterostructures with sharp band edges can be built at the single-layer limit using TMDC building blocks, which is a unique feature of this material system.

The nature of the photoluminescence of the WSe_2/MoS_2 hetero-bilayer is intriguing. To better understand the electronic structure of the hetero-bilayer, we performed absorption measurements in the near-infrared and visible part of the spectrum using synchrotron light shown as dashed lines in Fig. 3*B*. The WSe_2/MoS_2 hetero-bilayer shows a first absorption peak at 1.65 eV and a second peak at 1.91 eV. These peaks closely coincide with the absorption peaks of single-layer WSe_2 and MoS_2, respectively. Interestingly, comparing the absorption spectra with the normalized PL data shown in Fig. 3*B*, we note that the hetero-bilayer exhibits a striking ∼100 meV shift between the PL and absorbance peaks. This large Stokes-like shift is consistent with a spatially indirect transition in a staggered gap (type II) heterostructure (31) (as shown in Fig. 3*C*). Our hetero-bilayers share certain similarities with organic semiconductor heterostructures in which donor and acceptor layers are also bound by weak intermolecular vdW forces (32). Similar to the optical processes in organic heterostructures, photons are absorbed in single-layer WSe_2 and single-layer MoS_2, generating excitons in both layers. Photo-excited excitons then relax at the MoS_2/WSe_2

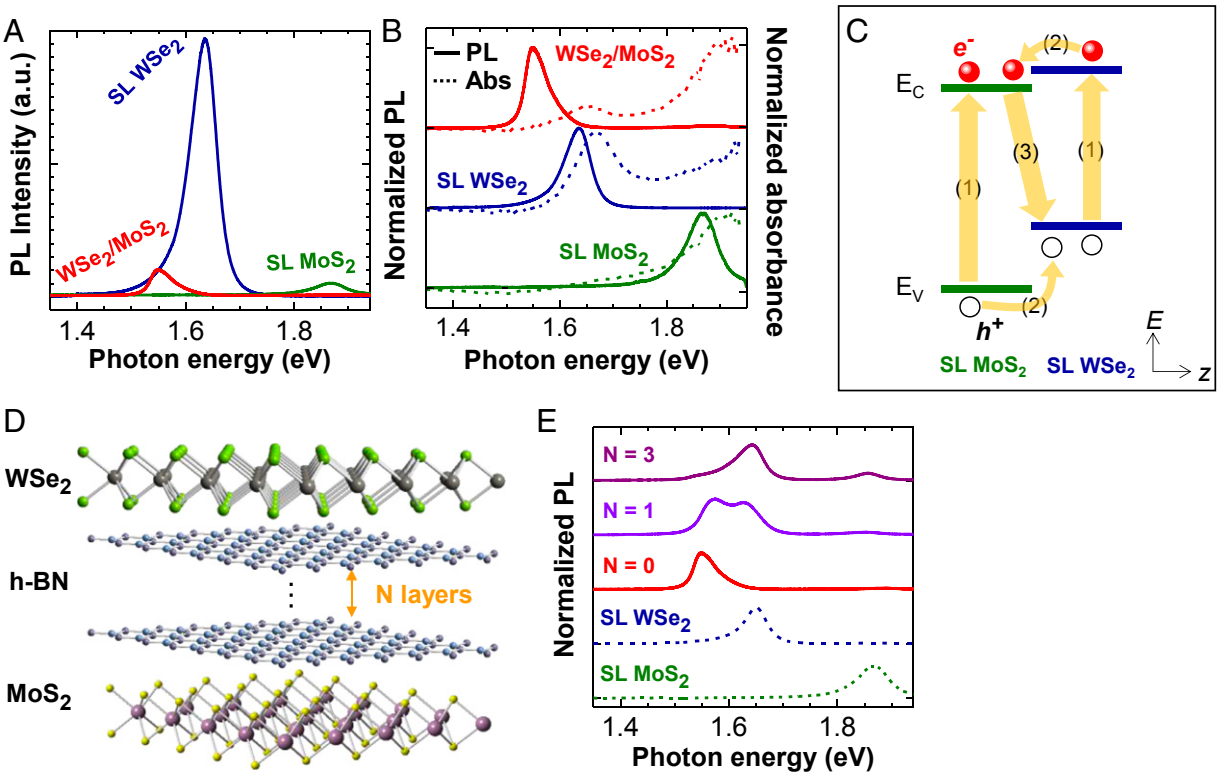

Fig. 3. Photoluminescence and absorption from WSe_2/MoS_2 hetero-bilayers. (*A*) PL spectra of single-layer WSe_2, MoS_2, and the corresponding hetero-bilayer. (*B*) Normalized PL (solid lines) and absorbance (dashed lines) spectra of single-layer WSe_2, MoS_2, and the corresponding hetero-bilayer, where the spectra are normalized to the height of the strongest PL/absorbance peak. (*C*) Band diagram of WSe_2/MoS_2 hetero-bilayer under photo excitation, depicting (1) absorption and exciton generation in WSe_2 and MoS_2 single layers, (2) relaxation of excitons at the MoS_2/WSe_2 interface driven by the band offset, and (3) radiative recombination of spatially indirect excitons. (*D*) An atomistic illustration of the heterostructure of single-layer WSe_2/single-layer MoS_2 with few-layer h-BN spacer in the vdW gap. (*E*) Normalized PL spectra from single-layer WSe_2/single-layer MoS_2 heterostructure with *n* layers of h-BN (n = 0, 1, and 3).

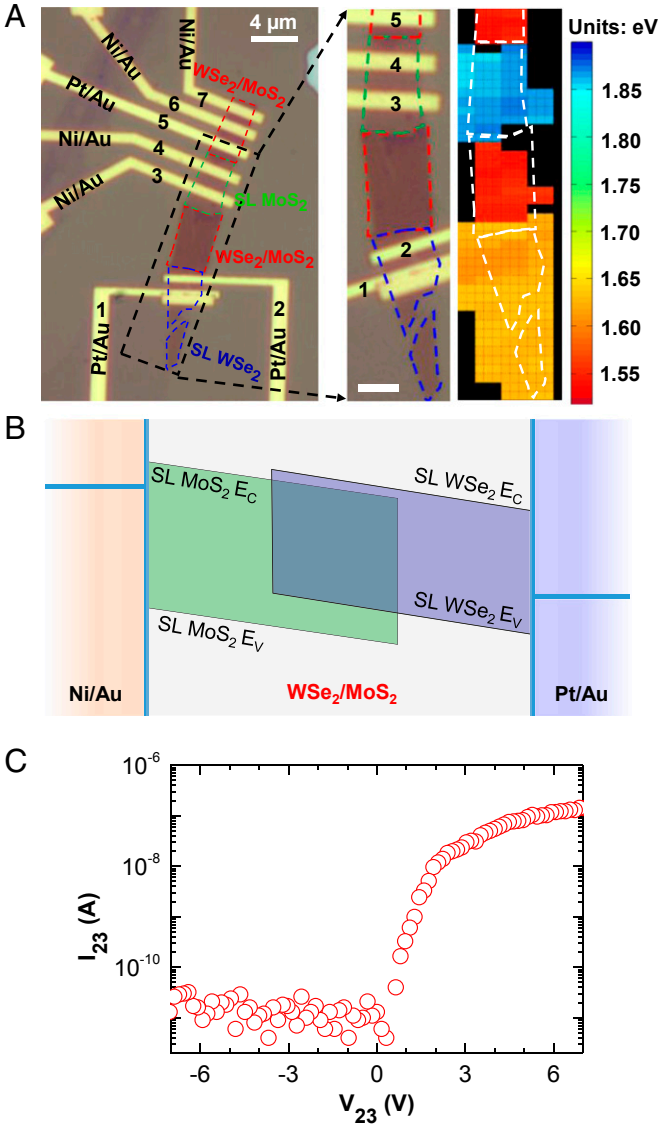

Fig. 4. Electrical transport across the WSe_2/MoS_2 hetero-interface. (*A*) Optical microscope image of a device encompassing single-layer WSe_2, WSe_2/MoS_2 hetero-bilayer, and single-layer MoS_2 on a Si/SiO_2 substrate. Electrodes are numbered 1–7 from bottom to top. (*Right*) A color-coded PL peak energy map. (Scale bar, 2 μm.) (*B*) A qualitative band diagram of the single-layer WSe_2/hetero-bilayer/single-layer MoS_2 device, corresponding to the device between electrodes 2 and 3. (*C*) I-V characteristic when measuring between electrodes 2 and 3, with 2 grounded and 3 biased. A back-gate voltage of 50 V was applied to reduce the contact resistance to MoS_2 and patterned NO_2 doping was used near the WSe_2 contact for reducing the contact resistance.

interface, driven by the band offset as shown in Fig. 3*C*. That band offset is also consistent with the measured built-in electric field from PEEM. Owing to the energy lost to the band offset (Fig. 3*C*), the PL excitonic peak energy is lower than the excitonic band gaps of either material component. This 100-meV shift may be a balance between conduction band offset between the two monolayers versus diminished exciton binding energy associated with being spatially indirect. Note that in the hetero-bilayer we observe only a weak luminescence signal at the energies corresponding to the excitonic band gaps of single-layer MoS_2 and WSe_2, suggesting that the large majority of the photo-excited carriers are relaxed at the interface producing the highest luminescence for the spatially indirect recombination process.

To fine-tune the interlayer interaction in the WSe_2/MoS_2 hetero-bilayer, single- and few-layer sheets of hexagonal BN (h-BN) spacer layers were inserted into the vdW gap (Fig. 3*D*) using the same transfer technique. Fig. 3*E* shows the normalized PL of hetero-stacks with single- and trilayer h-BN spacers. Interlayer spatially indirect recombination becomes negligible for the sample with a trilayer h-BN spacer, as indicated by both the position and the intensity of the peak at 1.64 eV (Fig. 3*E* and Fig. S6), which are nearly the same as for single-layer WSe_2. However, a single layer of h-BN does not fully suppress the interlayer interaction between WSe_2 and MoS_2. The results demonstrate that the interlayer coupling can be readily tuned by intercalation of dielectric layers and provide yet another degree of control in the vdW heterostructure properties.

Finally, we explored the carrier transport along the hetero-bilayer interface. A single flake consisting of single-layer WSe_2 and MoS_2, and an overlapping hetero-bilayer was made via the transfer process. The flake was dry etched into a long ribbon (Fig. 4*A*). A corresponding PL peak energy map is shown at the right edge of Fig. 4*A*, further depicting the ribbon structure by color coding of the luminescence energy. Multiple source/drain (S/D) metal electrodes were then fabricated by electron beam lithography and lift-off on each region of the ribbon (see Figs. S7 and S8 for details). The Si/SiO_2 substrate serves as the global back gate, with 260 nm gate oxide thickness. As expected single-layer MoS_2 and WSe_2 devices exhibit n- and p-channel characteristics, respectively (Fig. S9), consistent with previous reports (2, 3). However, the device consisting of one contact on the monolayer WSe_2 and the other on monolayer MoS_2, with the two layers overlapping in the central region (Fig. 4*B*) exhibits a distinct rectifying behavior (Fig. 4*C* and Fig. S10), consistent with type II band alignment of the hetero-bilayer. The rectification provides additional evidence for electrical coupling and proper contact potential between the two constituent layers. This behavior is consistent with previous work on TMDC/nanotubes (33) and TMDC/III-V heterostructures (34), which had shown that electrically active vdW interfaces can be achieved from TMDC components. The work here highlights the ability to engineer a novel class of electronic and optoelectronic devices by vdW stacking of the desired layered chalcogenide components with molecular-scale thickness control.

In summary, we have fabricated and characterized an artificial vdW heterostructure by stacking monolayer TMDC building blocks and achieved electronic coupling between the two 2D semiconductor constituents. Strong PL with a large Stokes-like shift was observed from the WSe_2/MoS_2 hetero-bilayer, consistent with spatially indirect luminescence from a type II hetero-structure. We anticipate that our result will trigger subsequent studies focused on the bottom-up creation of new hetero-structures by varying chemical composition, interlayer spacing, and angular alignment. In addition, the focus will be on the fabrication of vdW semiconductor heterostructure devices with tuned optoelectronic properties from customized single-layer components. Particularly, electroluminescene efficiency of vdW heterostructures needs to be explored experimentally to examine their viability for use as nanoscale light-emitting/lasing devices.

ACKNOWLEDGMENTS. Materials characterization of this work was supported by the director, Office of Science, Office of Basic Energy Sciences, Materials Sciences and Engineering Division of the US Department of Energy (DOE) under Contract DE-AC02-05CH11231. The device fabrication and characterization was supported by the National Science Foundation (NSF) E^3S center. The transmission electron microscopy work was performed at the National Center for Electron Microscopy, Lawrence Berkeley National Laboratory, which is supported by US DOE Contract DE-AC02-05CH11231. The absorption measurements were performed at the Advanced Light Source, Lawrence Berkeley National Laboratory. C. Carraro and R.M. acknowledge support from NSF Grant EEC-0832819 (Center of Integrated Nanomechanical Systems).

1. Mak KF, Lee C, Hone J, Shan J, Heinz TF (2010) Atomically thin MoS_2: A new direct-gap semiconductor. *Phys Rev Lett* 105(13):136805.
2. Radisavljevic B, Radenovic A, Brivio J, Giacometti V, Kis A (2011) Single-layer MoS_2 transistors. *Nat Nanotechnol* 6(3):147–150.
3. Fang H, et al. (2012) High-performance single layered WSe_2 p-FETs with chemically doped contacts. *Nano Lett* 12(7):3788–3792.
4. Wang H, et al. (2012) Integrated circuits based on bilayer MoS_2 transistors. *Nano Lett* 12(9):4674–4680.
5. Zeng H, Dai J, Yao W, Xiao D, Cui X (2012) Valley polarization in MoS_2 monolayers by optical pumping. *Nat Nanotechnol* 7(8):490–493.
6. Jones AM, et al. (2013) Optical generation of excitonic valley coherence in monolayer WSe_2. *Nat Nanotechnol* 8(9):634–638.
7. Geim AK, Grigorieva IV (2013) Van der Waals heterostructures. *Nature* 499(7459): 419–425.
8. Yu WJ, et al. (2013) Vertically stacked multi-heterostructures of layered materials for logic transistors and complementary inverters. *Nat Mater* 12(3):246–252.
9. Georgiou T, et al. (2013) Vertical field-effect transistor based on graphene-WS_2 heterostructures for flexible and transparent electronics. *Nat Nanotechnol* 8(2):100–103.
10. Yu WJ, et al. (2013) Highly efficient gate-tunable photocurrent generation in vertical heterostructures of layered materials. *Nat Nanotechnol* 8(12):952–958.
11. Britnell L, et al. (2013) Strong light-matter interactions in heterostructures of atomically thin films. *Science* 340(6138):1311–1314.
12. Wilson J, Yoffe A (1969) The transition metal dichalcogenides discussion and interpretation of the observed optical, electrical and structural properties. *Adv Phys* 18(73):193–335.
13. Terrones H, López-Urías F, Terrones M (2013) Novel hetero-layered materials with tunable direct band gaps by sandwiching different metal disulfides and diselenides. *Sci Rep* 3:1549.
14. Kang J, Li J, Li S-S, Xia J-B, Wang L-W (2013) Electronic structural Moiré pattern effects on MoS_2/$MoSe_2$ 2D heterostructures. *Nano Lett* 13(11):5485–5490.
15. Kośmider K, Fernández-Rossier J (2013) Electronic properties of the MoS_2-WS_2 heterojunction. *Phys Rev B* 87(7):075451.
16. Komsa H-P, Krasheninnikov AV (2013) Electronic structures and optical properties of realistic transition metal dichalcogenide heterostructures from first principles. *Phys Rev B* 88(8):085318.
17. Gong C, et al. (2013) Band alignment of two-dimensional transition metal dichalcogenides: Application in tunnel field effect transistors. *Appl Phys Lett* 103(5):053513.
18. Dean CR, et al. (2010) Boron nitride substrates for high-quality graphene electronics. *Nat Nanotechnol* 5(10):722–726.
19. Ponomarenko L, et al. (2011) Tunable metal-insulator transition in double-layer graphene heterostructures. *Nat Phys* 7(12):958–961.
20. Haigh SJ, et al. (2012) Cross-sectional imaging of individual layers and buried interfaces of graphene-based heterostructures and superlattices. *Nat Mater* 11(9): 764–767.
21. Britnell L, et al. (2012) Field-effect tunneling transistor based on vertical graphene heterostructures. *Science* 335(6071):947–950.
22. Gorbachev R, et al. (2012) Strong Coulomb drag and broken symmetry in double-layer graphene. *Nat Phys* 8:896–901.
23. Hunt B, et al. (2013) Massive Dirac fermions and Hofstadter butterfly in a van der Waals heterostructure. *Science* 340(6139):1427–1430.
24. Ponomarenko LA, et al. (2013) Cloning of Dirac fermions in graphene superlattices. *Nature* 497(7451):594–597.
25. Dean CR, et al. (2013) Hofstadter's butterfly and the fractal quantum Hall effect in moiré superlattices. *Nature* 497(7451):598–602.
26. Yankowitz M, et al. (2012) Emergence of superlattice Dirac points in graphene on hexagonal boron nitride. *Nat Phys* 8(5):382–386.
27. Zeng H, et al. (2013) Optical signature of symmetry variations and spin-valley coupling in atomically thin tungsten dichalcogenides. *Sci Rep* 3:1608.
28. Zhao W, et al. (2013) Evolution of electronic structure in atomically thin sheets of WS_2 and WSe_2. *ACS Nano* 7(1):791–797.
29. Van Roosbroeck W, Shockley W (1954) Photon-radiative recombination of electrons and holes in germanium. *Phys Rev* 94(6):1558.
30. Kost A, Lee H, Zou Y, Dapkus P, Garmire E (1989) Band-edge absorption coefficients from photoluminescence in semiconductor multiple quantum wells. *Appl Phys Lett* 54(14):1356–1358.
31. Wilson BA (1988) Carrier dynamics and recombination mechanisms in staggered-alignment heterostructures. *IEEE J Quantum Electron* 24(8):1763–1777.
32. Li G, Zhu R, Yang Y (2012) Polymer solar cells. *Nat Photonics* 6(3):153–161.
33. Jariwala D, et al. (2013) Gate-tunable carbon nanotube-MoS_2 heterojunction p-n diode. *Proc Natl Acad Sci USA* 110(45):18076–18080.
34. Chuang S, et al. (2013) Near-ideal electrical properties of InAs/WSe_2 van der Waals heterojunction diodes. *Appl Phys Lett* 102(24):242101.

Supporting Information

Fang et al. 10.1073/pnas.1405435111

SI Methods

Sample Preparation. Fabrication of the heterostructure started with the transfer of MoS_2, WSe_2, and hexagonal BN (h-BN) single and few layers on separate Si/SiO_2 substrates (oxide thickness, $t_{ox} = 260$ nm) using adhesive tapes by the mechanical exfoliation method (1). For h-BN, a 550-nm band-pass filter (FWHM 40 nm) was used to further enhance the optical contrast for locating single- to few-layer flakes on Si/SiO_2. These mechanically exfoliated flakes were then annealed at 250 °C for 3 h in a H_2 environment (3.3 torr, 200 sccm) to remove any surface organic residues. The heterostructures were realized by a dry transfer technique (2, 3) with a polymethyl methacrylate (PMMA) membrane as the transfer media. For the heterostructures with single- or few-layer h-BN, single-layer WSe_2 was first transferred onto h-BN, and then these two layers together were picked up by PMMA and transferred onto single-layer MoS_2.

Samples for transmission electron microscopy (TEM) were prepared on Au TEM grids with holey carbon nets of 1.2-μm-diameter orthogonal hole arrays (Ted Pella, Inc.). To remove the PMMA after transfer, the grids with the heterostructure/PMMA were immersed into dichloromethane (DCM) for 6 s, taken out to allow to air-dry for 3 min in fume hoods, and then annealed in H_2 with the same condition noted previously. The short time of immersion is to prevent the samples from escaping from the carbon net, whereas no blow dry was involved to keep the mechanical integrity of the relatively fragile carbon net. Samples for photoemission electron microscopy (PEEM) were prepared on natively oxidized p+ Si substrate. A similar cleaning process was used to remove PMMA and its residue as described above.

TEM Condition. The high-resolution TEM (HRTEM) image displayed in Fig. 1*C* was acquired on a FEI Titan microscope equipped with a field emission gun operating at accelerating voltage of 300 kV. The images were recorded on a 2,048 × 2,048 Gatan Ultrascan CCD camera using DigitalMicrograph software. The microscope was operated in low-dose mode to minimize electron beam-induced degradation as well as contamination of the sample. A Wiener-type filter was applied to the images to reduce the signal arising from the amorphous background. The electron diffraction pattern shown in Fig. 1*D* was acquired on a Zeiss Libra 200MC equipped with a monochromator and omega-type in-column energy filter using a 2,048 × 2,048 Gatan Ultrascan CCD camera. The microscope was operated at 200-kV accelerating voltage in parallel illumination mode with a semiconvergence angle of 40 μrad. The illuminated area was limited to 0.13 μm^2 using a condenser aperture with a diameter of 37 μm. Energy-filtered diffraction patterns were acquired and analyzed quantitatively using the dedicated software DigitalMicrograph.

Photoemission Electron Microscopy Experiments. The photoemission electron microscopy (PEEM) experiment was conducted at the soft X-ray undulator beamline UE49-PGM-a of the BESSY-II storage ring in Berlin using elliptically polarized light at photon energies of 700 eV and 150 eV. The endstation was equipped with an Elmitec PEEM-II energy microscope/analyzer allowing energy and spatially resolved imaging. Depending on the measured sample area, fields of view between 10 and 70 μm were used, resulting in a spatial resolution better than 30 and 120 nm, respectively. The total energy resolution of our measurements was 100 meV.

Optical Measurements. Photoluminescence (PL) and Raman measurements were performed at room temperature under ambient conditions. The samples were excited with a continuous-wave blue laser (473 nm) with a spot size of ∼1 μm, unless mentioned otherwise. The original laser power was 5 mW and neutral density filters were used with optical densities of 3 and 4 (corresponding to 5- and 0.5-μW laser power on the sample). Near-IR/visible absorption measurements were performed at Beamline 1.4.3 at the Advanced Light Source using a Nicolet Magna 760 FTIR interferometer and a Nicolet Nic-Plan infrared microscope. To access the visible region, all measurements used a quartz beamsplitter and a silicon detector (Thorlabs, Inc.). The use of synchrotron radiation enabled a spot size of <2 μm.

Details of the Hetero-Bilayer Device Fabrication. Following the fabrication of the WSe_2/MoS_2 hetero-bilayer, a single flake was dry-etched into a long ribbon with different regions corresponding to single-layer WSe_2, MoS_2, and hetero-bilayer. Pt/Au and Ni/Au metal contacts were then placed on single- layer WSe_2 and single-layer MoS_2 regions, respectively. A ZrO_2 layer was deposited onto single-layer MoS_2 region and partial hetero-bilayer region in the ribbon. The device was finally measured with NO_2 doping on the exposed WSe_2 region to minimize contact resistance at the Pt/WSe_2 contact, as shown in Fig. S7. Note that without NO_2 doping the device still exhibits rectifying behavior with ∼10 times lower forward bias current density arising from the extra parasitic resistances (Fig. S8). The step-by-step fabrication process is as follows.

i) E-beam lithography was used to define etched regions in the hetero-bilayer flake. Briefly, samples were coated with PMMA (4% in chlorobenzene), baked at 180 °C for 5 min, and then exposed using an electron-beam lithography system.

ii) The hetero-bilayer flakes were then patterned dry-etched using XeF_2/N_2 gas (XeF_2 3 torr, N_2 1.5 torr). For eight cycles of 30 s of etching, the etch rate of chalcogenides is over 10 nm/min.

iii) The PMMA mask was removed by a DCM wash for 10 min and the samples were then annealed in H_2 (3.3 torr, 200 sccm) for 3 h to remove the PMMA residue.

iv) Ni/Au (10 nm/30 nm) contacts were deposited on single-layer MoS_2 region by an e-beam lithography, metal deposition, and lift-off process. Ni/Au was chosen to contact MoS_2 because it is known to enable efficient injection of electrons (4, 5). A short Ni/Au "anchor" bar (∼5 μm in length) was also deposited at the end of WSe_2 side to prevent the flake detaching from the substrate during the lift-off process.

v) Pt/Au (10 nm/30 nm) contacts were deposited on single-layer WSe_2 region by a similar e-beam lithography, metal deposition, and lift-off process. Pt/Au was found to give better p-type conduction in single-layer WSe_2 than Pd, which was the best contact to the valence band of WSe_2 (6).

vi) A ZrO_2 layer (20 nm) was then deposited onto single-layer MoS_2 region and partial hetero-bilayer region in the ribbon as a NO_2 blocker by an e-beam lithography, atomic layer deposition, and lift-off process.

vii) The fully fabricated device was then exposed to 0.05% NO_2 in N_2 gas for 10 min and measured, as shown in Fig. S7. For the I-V characteristic shown in Fig. 4*C* in the main text, a back-gate voltage of 50 V was applied to lower the parasitic resistance from MoS_2 while the parasitic WSe_2 was still degenerately p-doped (6).

TEM Analysis

The lattice constants of the real lattices can be calculated from

$$\frac{1}{d^2}=\frac{4}{3}\frac{h^2+k^2+hk}{a^2},$$

where d is the length of the reciprocal lattice vector of the crystal lattice planes of ($hk0$) and a is the lattice constant of the chalcogenide crystal. This calculation yields a value of (4.4 ± 0.1)% for the lattice mismatch between the WSe_2 single layer and the underneath MoS_2 single layer, which is nearly identical to their bulk value. The alignment of the two lattices can also be examined with a fast Fourier transform of the two zoomed-in TEM images in Fig. 1*C* in the main text, as shown in Fig. S1.

Raman Characterization of the WSe_2/MoS_2 Hetero-Bilayer

There are four Raman-active modes for both WSe_2 and MoS_2, of which only A_{1g} and E^1_{2g} modes were observed in our measurements owing to the selection rule in the back-scattering configuration and the restricted rejection against Rayleigh scattering (7). As shown in Fig. S2, the in-plane E^1_{2g} mode peaks of WSe_2 and MoS_2 remained unchanged (within 0.5 cm^{-1}) comparing before and after transferring. This is a clear indication that there is no/negligible strain in either layer in the final hetero-bilayer, consistent with our TEM analysis. The out-of-plane A_{1g} mode peak red-shifted by ∼1 cm^{-1} (from 405.1 cm^{-1} to 404.1 cm^{-1}) for MoS_2, whereas for WSe_2 it is hard to detect because the A_{1g} peak is overlapping with the E^1_{2g} peak. This small red shift should be attributed to the interlayer coupling, which is also seen in bulk/few-layer WSe_2 and MoS_2 (7, 8).

PEEM Experiment Detail

As shown in Fig. S3*A*, a WSe_2/MoS_2 hetero-stack, which contained a single-layer WSe_2 on top of MoS_2 with thicknesses ranging from one single layer to two single layers and four single layers was measured and analyzed by PEEM. Note that the thicknesses of the layers were determined by optical contrast, atomic force microscope in combination with PL. Fig. S3*B* shows the W $4f_{7/2}$ binding energy position contour, where distinct boundaries between regions can be visualized and are consistent with our sample geometry. The binding energy map was obtained by a batch-fitting of all spectra collected at different detector locations; single peaks of W $4f_{7/2}$ and Mo $3d_{5/2}$ were simulated by a Gaussian profile. For more precise analysis, signals from homogeneous parts of the image were spatially integrated and more sophisticated fitting procedure (a combination of Shirley background and Doniach–Sunjic lineshape) was used (Fig. 2). For the single-layer WSe_2 in contact with the substrate, the W $4f_{7/2}$ binding energy is 33.78 eV, whereas for the single-layer WSe_2 on top of single-layer MoS_2 the W $4f_{7/2}$ binding energy is 33.56 eV. The W $4f_{7/2}$ core level binding energy decreased by ∼220 meV when contacting to MoS_2, as noted in the text. The direction of the peak shift is consistent with a negative net charge on the WSe_2 in the WSe_2/MoS_2 hetero-bilayer, as predicted by density functional theory (9). However, charge neutrality in the hetero-bilayer requires that a shift in the opposite direction be present on the MoS_2 component of WSe_2/MoS_2. As is shown in Fig. S3*C*, a shift of +190 meV with respect to stand-alone MoS_2 is indeed observed in the Mo 3d core levels of the WSe_2/MoS_2 (from 227.26 eV to 227.45 eV). The shifts in the W and Mo core levels are evidence that there exists a charge transfer-induced electric field between WSe_2 and MoS_2 layers. The hetero-bilayer can essentially be interpreted as being a 2D dipole, an atomically thin parallel plate capacitor with van der Waals gap. One can also notice that the W $4f_{7/2}$ binding energy position shifted less when contacting to thicker MoS_2 layers by ∼30 meV per layer. It is not clear at this stage which one of the three parameters, namely, the charge-transfer amount, layer distance, or the dielectric constant in the van der Waals gap, is playing a more important role in this slight decrease. Detailed density functional theory calculations are needed to further shed light on this issue.

Luminescence Tail Analysis

The band edge tail $D(\nu)$ as a function of frequency ν [also called the Urbach tail (10)], is related to the photon emission rate per unit energy by the van Roosbroeck–Shockley equation (11, 12). $D(\nu)$ can further be related to the photoluminescence spectrum $I(\nu)$ by

$$D(\nu)\propto\frac{I(\nu)\left(e^{h\nu/kT}-1\right)}{n_r^2\nu^2},$$

where h is Planck's constant, k is Boltzmann's constant, T is temperature, and n_r is the real part of the refractive index. Fig. S5 shows the shapes of the Urbach tails of single-layer WSe_2, single-layer MoS_2, and the WSe_2/MoS_2 hetero-bilayer. An optical semilog inverse slope of 30 meV/dec is extracted from all three tails, corresponding to the sharpness of the band edge. The nearly identical inverse slope of the hetero-bilayer proves that the band edge sharpness of the heterostructure can be as high as that of its constituent single layers.

Absolute PL Spectra of WSe_2/MoS_2 Heterostructure with h-BN

Fig. S6 shows the absolute PL of WSe_2/MoS_2 hetero-stacks with single- and trilayer h-BN spacers, along with the PL of single-layer WSe_2. Interlayer coupling becomes negligible for the sample with a trilayer h-BN spacer, as indicated by both the position and the intensity of the peak at 1.64 eV, which are nearly the same as single-layer WSe_2. The slight difference (0.01 eV) in the peak position is likely due to the fact that the boundary on the bottom side of WSe_2 has changed from SiO_2 to h-BN. On the other band, a single layer of h-BN does not fully suppress the interlayer interaction between WSe_2 and MoS_2. The PL spectrum of WSe_2/h-BN/MoS_2 shows a double peak feature centered at 1.6 eV with an intensity on the order of one-third of that of typical single-layer WSe_2. We interpret the lower energy peak component of the doublet as being the peak of the hetero-bilayer with reduced interlayer coupling owing to the intercalation of the h-BN single layer. Indeed, this peak falls in between the peak of the unperturbed single-layer WSe_2 and strongly coupled WSe_2/MoS_2 bilayer. This demonstrates that the interlayer coupling can be readily tuned by intercalation of layered dielectric media into the van der Waals gap. The higher energy peak closely coincides with the peak of single-layer WSe_2 and could be due to a competing spatially direct emission in single-layer WSe_2 as the photo-generated electrons now see a BN barrier and would have certain probability of staying in the excitonic conduction band edge of WSe_2. This interpretation is also supported by the weak emission close to the position of single-layer MoS_2.

1. Novoselov KS, et al. (2004) Electric field effect in atomically thin carbon films. *Science* 306(5696):666–669.
2. Dean CR, et al. (2010) Boron nitride substrates for high-quality graphene electronics. *Nat Nanotechnol* 5(10):722–726.
3. Ponomarenko L, et al. (2011) Tunable metal-insulator transition in double-layer graphene heterostructures. *Nat Phys* 7(12):958–961.
4. Fang H, et al. (2013) Degenerate n-doping of few-layer transition metal dichalcogenides by potassium. *Nano Lett* 13(5):1991–1995.

5. Liu H, Neal AT, Ye PD (2012) Channel length scaling of MoS_2 MOSFETs. *ACS Nano* 6(10):8563–8569.
6. Fang H, et al. (2012) High-performance single layered WSe_2 p-FETs with chemically doped contacts. *Nano Lett* 12(7):3788–3792.
7. Zeng H, et al. (2013) Optical signature of symmetry variations and spin-valley coupling in atomically thin tungsten dichalcogenides. *Sci Rep* 3:1608.
8. Lee C, et al. (2010) Anomalous lattice vibrations of single- and few-layer MoS_2. *ACS Nano* 4(5):2695–2700.
9. Terrones H, López-Urías F, Terrones M (2013) Novel hetero-layered materials with tunable direct band gaps by sandwiching different metal disulfides and diselenides. *Sci Rep* 3:1549.
10. Urbach F (1953) The long-wavelength edge of photographic sensitivity and of the electronic absorption of solids. *Phys Rev* 92:1324.
11. Van Roosbroeck W, Shockley W (1954) Photon-radiative recombination of electrons and holes in germanium. *Phys Rev* 94(6):1558.
12. Kost A, Lee H, Zou Y, Dapkus P, Garmire E (1989) Band-edge absorption coefficients from photoluminescence in semiconductor multiple quantum wells. *Appl Phys Lett* 54(14):1356–1358.

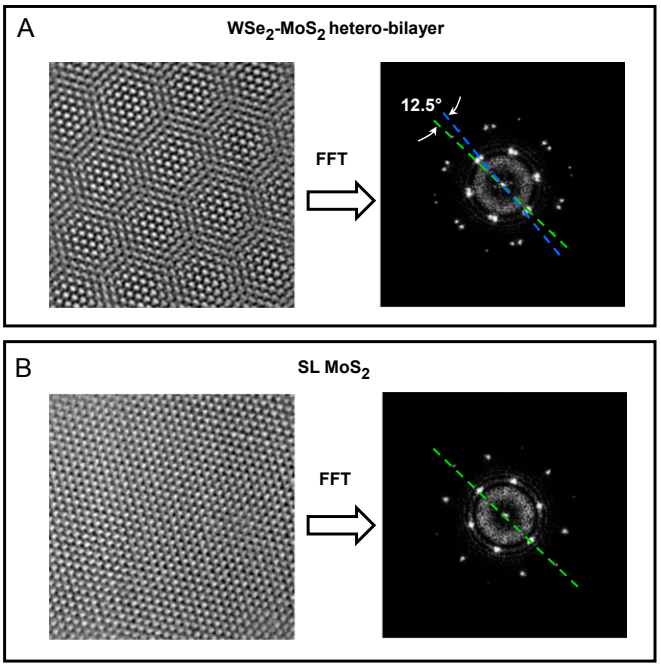

Fig. S1. Fast Fourier transform of the HRTEM images shown in Fig. 1*C* in the main text for (*A*) WSe_2/MoS_2 hetero-bilayer and (*B*) single-layer MoS_2.

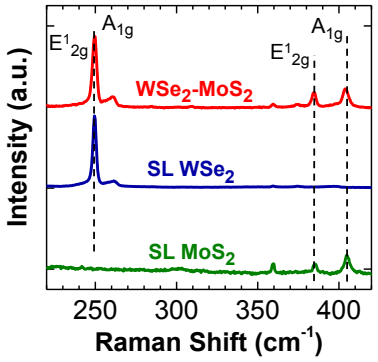

Fig. S2. Raman spectra comparison for single-layer MoS_2 and WSe_2 and the WSe_2/MoS_2 hetero-bilayer. The excitation laser wavelength here is 532 nm.

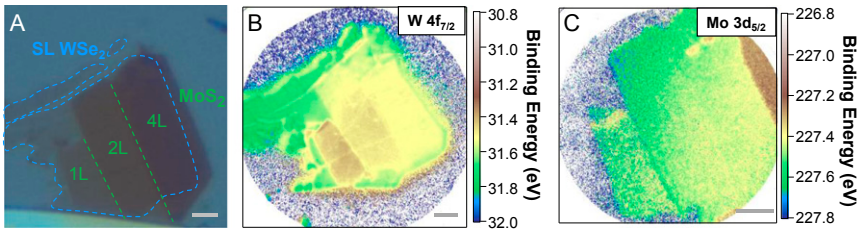

Fig. S3. (*A*) The optical microscope image of the WSe_2/MoS_2 heterostructure for PEEM characterization. The PEEM sample was on a naturally (native) oxidized heavily p-doped Si substrate, and the image was taken when the sample was on Si/SiO_2 (260 nm) substrate. (*B*) W $4f_{7/2}$ binding energy position contour plot of the sample in *A*. (*C*) Mo $3d_{5/2}$ binding energy position contour plot of the sample in *A*. (Scale bars, 2 μm.)

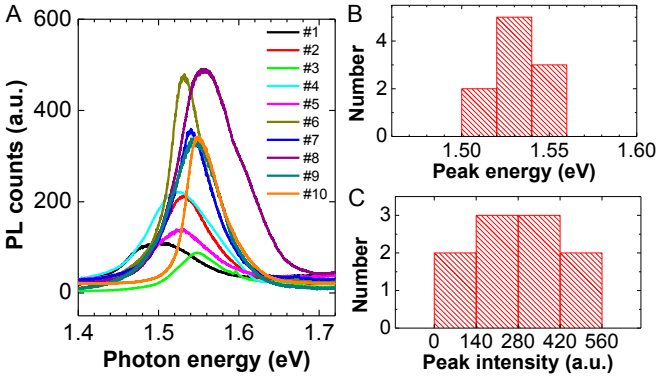

Fig. S4. PL statistics of multiple WSe_2/MoS_2 hetero-bilayer samples. (*A*) PL spectra of 10 WSe_2/MoS_2 hetero-bilayers. (*B*) Histogram of the PL peak energies for these 10 samples. (*C*) Histogram of the PL peak intensities for these 10 samples.

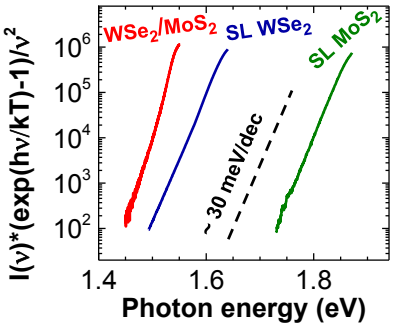

Fig. S5. Band edge tails derived from the PL using the van Roosbroeck–Shockley equation, depicting the sharpness of the band edges. The spectra were normalized to peak magnitude.

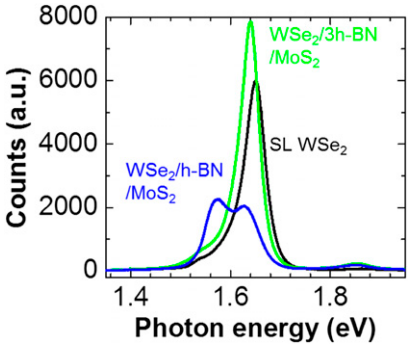

Fig. S6. Absolute PL comparison of single-layer WSe_2, single-layer WSe_2/single-layer MoS_2 heterostructure with single- and trilayer h-BN in between.

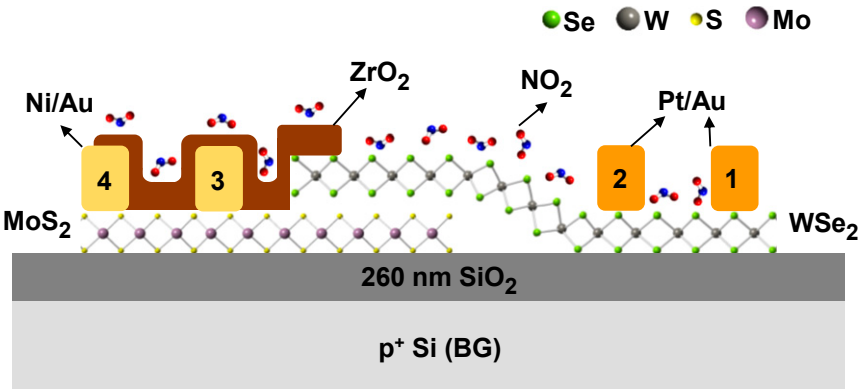

Fig. S7. Schematic of fully fabricated WSe_2/MoS_2 hetero-bilayer device. NO_2 doping of exposed WSe_2 region was used to reduce the contact/parasitic resistances of WSe_2.

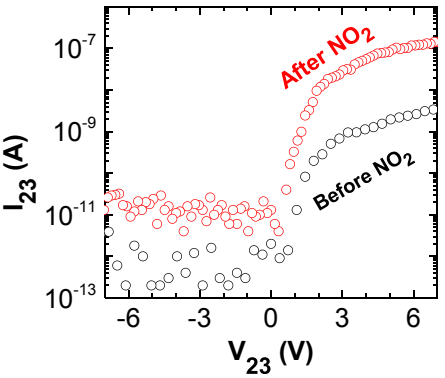

Fig. S8. I-V characteristic when measuring between electrodes 2 and 3 (with 2 grounded and 3 biased) before and after NO_2 doping of the exposed WSe_2 region in the WSe_2/MoS_2 hetero-bilayer device. A back-gate voltage of 50 V was applied.

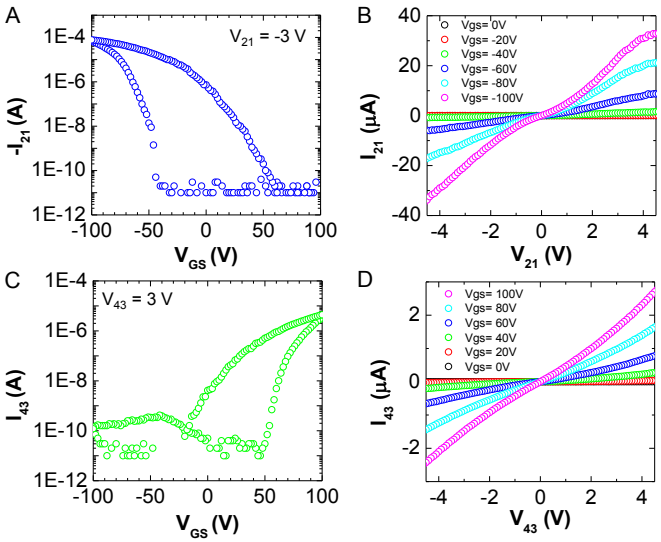

Fig. S9. (*A*) Transfer characteristic of the single-layer WSe_2 device in Fig. 4*A* of the main text (measured between terminals 1 and 2). (*B*) Output characteristic of the device in *A*. (*C*) Transfer characteristic of the single-layer MoS_2 device in Fig. 4*A* of the main text (measured between terminals 3 and 4). (*D*) Output characteristic of the device in *C*.

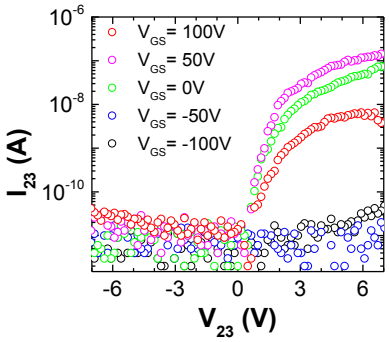

Fig. S10. Gate dependence in the I-V characteristic of WSe_2/MoS_2 heterojunction. Owing to the parasitic resistances in the WSe_2 and MoS_2 single layers, the I-V shows an "anti-ambiploar" behavior, namely, the peak conductance at the forward bias region appears near an intermediate gate bias, which is similar to what has been previously observed in the MoS_2/nanotubes heterostructure (1).

1. Jariwala D, et al. (2013) Gate-tunable carbon nanotube-MoS_2 heterojunction p-n diode. *Proc Natl Acad Sci USA* 110(45):18076–18080.